

Discrete quantum geometry and intrinsic spin Hall effect

Jie-Xiang Yu^{1,2}, Jiadong Zang,¹ Roger K. Lake,³ Yi Zhang⁴, and Gen Yin^{5,*}


¹*Department of Physics and Astronomy, University of New Hampshire, Durham, New Hampshire 03824, USA*

²*Department of Physics, Center for Molecular Magnetic Quantum Materials and Quantum Theory Project, University of Florida, Gainesville, Florida 32611, USA*

³*Department of Electrical and Computer Engineering, University of California, Riverside, California 92521, USA*

⁴*International Center for Quantum Materials, School of Physics, Peking University, Beijing 100871, China*

⁵*Department of Physics, Georgetown University, Washington, D.C. 20057, USA*

 (Received 16 June 2021; revised 26 October 2021; accepted 26 October 2021; published 4 November 2021)

We show that the quantum geometry of the Fermi surface can be numerically described by a three-dimensional discrete quantum manifold. This approach not only avoids singularities in the Fermi sea, but it also enables the precise computation of the intrinsic Hall conductivity resolved in spin, as well as any other local properties of the Fermi surface. The method assures numerical accuracy when the Fermi level is arbitrarily close to singularities, and it remains robust when Kramers degeneracy is protected by symmetry. The approach is demonstrated by calculating the anomalous Hall and spin Hall conductivities of a two-band lattice model of a Weyl semimetal and a full-band *ab initio* model of zinc-blende GaAs.

DOI: [10.1103/PhysRevB.104.184408](https://doi.org/10.1103/PhysRevB.104.184408)

It has been well established that the intrinsic anomalous (spin) Hall effect originates from the topological property of the Fermi sea, and it can be evaluated through an integral of the Berry curvature among the occupied states [1,2]. Such an approach has been employed for first-principles calculations in different ways [3–5]. A particularly convenient approach is Wannier interpolation [6], where a dense mesh in k space does not significantly increase the numerical complexity. One difficulty of such an approach are the singularities caused by band crossings. Such crossings, either accidental or protected by symmetry, result in sharp peaks of the anomalous Hall conductivity. This makes the numerical evaluation difficult, especially when the singularities are close to the Fermi surface, which usually cannot be avoided in a scan of the Fermi level.

An alternative and natural perspective is to describe the nonquantized part of the anomalous Hall effect as a geometric property of the Fermi surface [7]. This approach formulates the anomalous Hall conductivity as a surface integral of Berry curvature weighted by the Fermi wave vector \mathbf{k}_F , which naturally avoids singularities in the Fermi sea. The method has been implemented for full-band models by decomposing the integral on the Fermi surface into a sum of oriented Wilson loops [8,9]: $\sigma_{xy} \sim \sum_{n,i} k_{z,i} \phi_{n,i}$. Here, n is the band index, $k_{z,i}$ is the z component of \mathbf{k}_F on the i th slice, and $\phi_{n,i} = \oint^i \mathbf{A}_n \cdot d\mathbf{l}$ is the gauge-invariant Berry phase looping through the i th slice as schematically shown in Fig. 1(a). At the continuous limit, $\mathbf{A}_n = i \langle \psi_n^k | \nabla_{\mathbf{k}} | \psi_n^k \rangle$ is the Berry connection of the n th band. Numerically, the closed loops are decomposed into discrete Wilson links, such that $\phi_{n,i} = -\text{Im}[\ln \prod_j \langle j | j+1 \rangle]$, where $\langle j | j+1 \rangle$ is the inner product between two neighboring eigenstates associated with a segment of the loop. Although

$\phi_{n,i}$ is defined on $(-\pi, \pi]$, which seems arbitrary, one can enforce a smooth $\phi_{n,i}$ by carefully handling the branches of the Berry phase, such that $|\phi_{n,i} - \phi_{n,i+1}| \ll 2\pi$. Thus the Fermi-surface approach only contains an ambiguity with multiples of 2π compared to the Fermi-sea prescription, which corresponds to the undetermined quantized part of the Hall conductivity.

Although the aforementioned slice-based approach is promising, it cannot capture the intrinsic spin Hall effect. Obtained by the loop integral on each slice of the Fermi surface, the Berry phase is formulated as a global property. Namely, the spin-Hall conductivity can only be expressed as $\sigma_{xy}^{(\alpha)} \sim \sum_{n,i} s_{\alpha,i} k_{z,i} \phi_{n,i}$ where $s_{\alpha,i}$ is the uniform spin on slice i . This becomes problematic when strong spin-orbit coupling (SOC) occurs, where spins usually have a texture on the Fermi surface, and therefore must be evaluated locally. Furthermore, the slice-based approach requires the choice of k_z perpendicular to the x - y transport plane. Any rotation of the transport plane requires re-establishing the slices and re-evaluating the Berry phases $\{\phi_i\}$ for all slices. This is counterintuitive since the Fermi surface should contain enough information to determine the intrinsic (spin) Hall conductivity for arbitrary current directions.

In this paper, we show that the nonquantized part of the intrinsic anomalous (spin) Hall conductivity can be fully captured by a three-dimensional (3D) discrete quantum manifold of the Fermi surface. In such a manifold, Wilson links form local loops, as shown in Fig. 1(b), and therefore the Hall conductivity can be resolved in spin, as well as any other local properties of the Fermi surface. Such an approach can naturally handle singularities near the Fermi surface, and it remains robust when Kramers degeneracy is protected by symmetry. The approach is tested on a 2×2 tight-binding model of Weyl semimetal and an *ab-initio* full-band model of zinc-blende GaAs.

*gen.yin@georgetown.edu

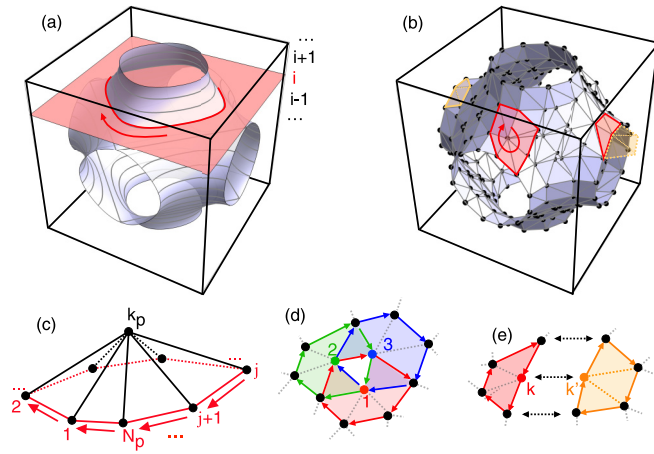


FIG. 1. Illustration of different approaches to describe intrinsic anomalous Hall effect as a geometric property of the Fermi surface. (a) The slice-based approach. The Fermi surface ($\epsilon_F = 0$) corresponds to a cubic tight-binding model $\epsilon_{\mathbf{k}} = -2t(\cos k_x + \cos k_y + \cos k_z)$, where t is the hopping between nearest neighbors. (b) The new vertex-based method by establishing a three-dimensional discrete manifold of the Fermi surface. (c) The local Berry phase associated with each vertex given by the adjacent triangles. (d) The flux of Berry curvature is over-counted by three times for Δ_{123} . (e) Manifold matching between vertices and edges on opposing Brillouin-zone boundaries. The red and orange polygons correspond to the ones shown in (b) near the boundaries.

At the limit of linear response, the nonequilibrium group velocity driven by an applied electric field \mathcal{E} contains two parts: $\mathbf{v} = \mathbf{v}_0 + \mathbf{v}_a$, where $\mathbf{v}_0 = \frac{1}{\hbar}\nabla_{\mathbf{k}}\epsilon$ is the regular group velocity and $\mathbf{v}_a = \frac{e}{\hbar}\mathcal{E} \times \boldsymbol{\Omega}_n(\mathbf{k})$ is the anomalous velocity. At zero temperature, the leading-order average of \mathbf{v}_a is

$$\langle \mathbf{v}_a \rangle = \frac{e\mathcal{E}}{\rho\hbar} \times \left(\frac{1}{2\pi} \right)^3 \sum_n \mathbf{I}_n \quad (1)$$

where ρ is the carrier density and n is the band index. Thus

$$\mathbf{I}_n = \int_{\text{BZ}} f_0 \boldsymbol{\Omega}_n d\mathbf{v} = \int_{\text{BZ}} f_0 (\nabla \times \mathbf{A}_n) d\mathbf{v}, \quad (2)$$

where f_0 is the equilibrium Fermi factor. At zero temperature, using integration by parts,

$$\mathbf{I}_n = \sum_{\alpha} \hat{n}_{\alpha} \times \int_{\text{BZB}} (f_0 \mathbf{A}_n) ds_{\alpha} + \int_{\text{BZ}} \delta(\epsilon - \epsilon_F) \nabla \epsilon \times \mathbf{A}_n d\mathbf{v} \quad (3)$$

where the first integral goes over Brillouin-zone boundaries (BZBs), and the second one is a volume integral within the Brillouin zone (BZ). Eq. (3) is equivalent to the one by Haldane [7]. Here, \hat{n}_{α} ($\alpha = 1, 2, \dots, 6$) is the normal vector of BZBs. For 3D crystals, one can choose a Brillouin zone with three pairs of opposing BZBs. For each pair, $\hat{n}_{\alpha} = -\hat{n}_{\beta}$, and the first term in Eq. (3) vanishes. As a result,

$$\mathbf{I}_n = \int_{\text{FS}} ds \times \mathbf{A}_n. \quad (4)$$

The manifold defined on a continuous Fermi surface is topologically equivalent to a discrete manifold as shown in Fig. 1(b). Such a manifold can be obtained by the marching

tetrahedra method. Once an intersection is detected between ϵ_F and a tetrahedron, the Fermi-surface piece must be an oriented triangle, since the normal vector can be defined along $\nabla_{\mathbf{k}}\epsilon_F$. The orientation of each triangle distinguishes electron and hole bands. The integration in Eq. (4) can thus be approximated by summing through the surface pieces:

$$\vec{\Delta} = \frac{1}{2}(\mathbf{k}_2 - \mathbf{k}_1) \times (\mathbf{k}_3 - \mathbf{k}_1) \times \mathbf{A} \approx \hat{n} \times \mathbf{A} ds \quad (5)$$

where \hat{n} is the normal vector, and the three vertices of the triangle are labeled by 1,2,3, following some convention of chirality with respect to \hat{n} . With some algebra,

$$\vec{\Delta} = \frac{1}{2}(w_{12}\mathbf{k}_3 + w_{23}\mathbf{k}_1 + w_{31}\mathbf{k}_2) \quad (6)$$

$$= \frac{1}{2}\mathbf{k}_1(w_{12} + w_{23} + w_{31}) + o(\mathbf{k}_1). \quad (7)$$

Here,

$$w_{\alpha\beta} = -\text{Im}[\mathbf{A} \cdot (\mathbf{k}_{\beta} - \mathbf{k}_{\alpha})] = -\text{Im}(\ln\langle \mathbf{k}_{\alpha} | \mathbf{k}_{\beta} \rangle) \quad (8)$$

is the Wilson link between two adjacent vertices, where $|\mathbf{k}_{\alpha}\rangle$ and $|\mathbf{k}_{\beta}\rangle$ are the corresponding eigenstates. The integral in Eq. (4) can therefore be written as

$$\mathbf{I}_n = \sum_i \vec{\Delta}_{n,i} = \frac{1}{6} \sum_p \mathbf{k}_{n,p} \phi_{n,p} \quad (9)$$

where i labels triangles and $\mathbf{k}_{n,p}$ is the k -space position of vertex p on in the n th shell of the Fermi surface. Here, $\phi_{n,p}$ is the gauge-invariant local Berry phase

$$\phi_{n,p} = -\text{Im} \left(\ln \prod_j^{N_p} \langle j, n | j+1, n \rangle \right), \quad (10)$$

where j goes through the vertices surrounding vertex p as shown in Fig. 1(c). The extra factor of $1/3$ in Eq. (9) comes from over-counting the Berry phase as shown in Fig. 1(d). The logarithm in Eq. (10) is defined on the branch of $(-\pi, \pi]$ with an unknown multiple of 2π . Such ambiguity can be naturally ruled out since the local Berry phase is close to zero piecewise. The Hall conductivity can then be obtained by $\sigma_{\mu\nu} = \frac{e^2}{\hbar} \left(\frac{1}{2\pi} \right)^3 \sum_n \mathbf{I}_n \cdot \hat{\lambda}$ for an arbitrary coordinate setup, where μ, ν and λ represent x, y and z in cyclic order.

The summation in Eq. (9) holds true for both the vertices inside the Brillouin zone and the ones on the BZBs. Defined in the affine \mathbf{k} space, the Fermi surface is periodic and the surface edges on opposing BZBs are therefore connected. This requires careful handling to ensure translational symmetry. As shown in Fig. 1(e), each boundary vertex \mathbf{k} must be paired with another vertex \mathbf{k}' on the opposing BZB, shifted by a reciprocal lattice vector. As a result, a closed Wilson loop can be formed for each boundary vertex by including the incoming and outgoing edges on the BZB. Mismatching of boundary vertices will result in topological defects of the discrete manifold, making it nonhomeomorphic with the continuous limit. Similar to the slice-based approach, Eq. (9) also leaves the quantized part of Hall conductivity undetermined. This can be seen by taking $\mathbf{k} \rightarrow \mathbf{k} + \mathbf{G}$ for all vertices, where \mathbf{G} is an arbitrary reciprocal lattice point.

The approach defined by Eqs. (9) and (10) enables the evaluation of intrinsic spin-Hall effect for materials with strong SOC. Since Eq. (9) sums through all vertices, each vertex

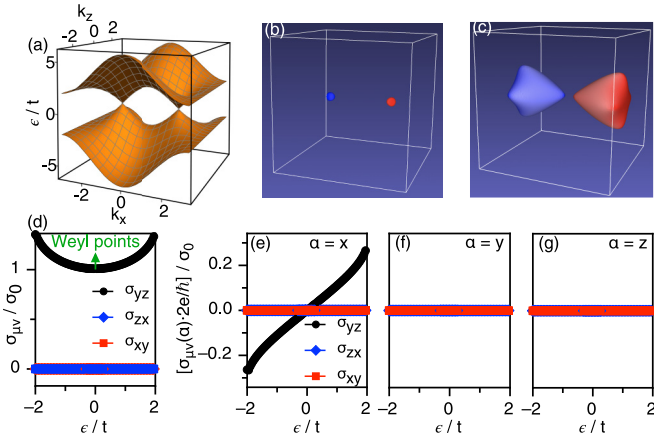


FIG. 2. Intrinsic (spin) Hall effect in a lattice model of a Weyl semimetal. (a) The band structure given by the model with $k_y = 0$, $k_0 = \frac{\pi}{2}$, $t_x = t$, and $m = 2t$. (b) Fermi surface obtained as a 3D discrete quantum manifold ($\epsilon_F = 0.45t$). The vertices are colored by the local Berry curvature. (c) The Fermi surface at $\epsilon_F = 1.05t$, where the shape represents the symmetry of the lattice. (d) The intrinsic anomalous Hall conductivity computed using Eqs. (9) and (10). Here, $\sigma_{\mu\nu}$ is normalized to the Weyl-point conductivity $\sigma_0 = e^2/2h$. (e) and (f) The intrinsic spin-Hall conductivity tensor evaluated using Eq. (11). The results are first converted to the corresponding electrical conductivity and then normalized to σ_0 .

can be resolved in any local properties such as the electron spin. As a result the intrinsic spin Hall conductivity can be straightforwardly obtained using

$$\langle \mathbf{v}_a s_\alpha \rangle = \frac{e\mathcal{E}}{\rho\hbar} \times \left(\frac{1}{2\pi} \right)^3 \sum_n \mathbf{I}_n^{(\alpha)}. \quad (11)$$

Here, $\langle \mathbf{v}_a s_\alpha \rangle$ is the expectation of the spin-velocity tensor, where s_α represents the Pauli matrices for electron spins ($\alpha = x, y, z$). For each band, the integral $\mathbf{I}_n^{(\alpha)}$ can be obtained by summing through all vertices $\mathbf{I}_n^{(\alpha)} = \frac{1}{6} \sum_p \mathbf{k}_{n,p} \phi_{n,p} \langle s_{\alpha,p} \rangle$, where n is the band index and $\langle s_{\alpha,p} \rangle$ is the spin expectation on vertex p . The spin Hall conductivity is then written as $\sigma_{\mu\nu}^{(\alpha)} = \left(\frac{1}{2\pi} \right)^3 \frac{e}{2} \sum_n \mathbf{I}_n^{(\alpha)} \cdot \hat{\lambda}$.

The vertex-based Fermi-surface approach remains well-defined when ϵ_F is arbitrarily close to point singularities of Berry curvature, i.e., Weyl points. We demonstrate this using a 2×2 tight-binding model of a Weyl semimetal:

$$H = s_x [m(2 - \cos k_y - \cos k_z) + 2t_x (\cos k_x - \cos k_0)] - 2ts_y \sin k_y - 2ts_z \sin k_z. \quad (12)$$

The first term breaks time-reversal symmetry, resulting in two Weyl points at $(\pm k_0, 0, 0)^T$ as shown in Fig. 2(a). When ϵ_F is close to the Weyl points, the Fermi surface contains approximately two spheres, each wrapping a sink and a source of the Berry curvature, respectively [Fig. 2(b)]. Away from the Weyl points, the Fermi surface is shown in Fig. 2(c), where the symmetry of the cubic lattice can be seen. Computed from Eq. (9), anomalous Hall conductivities along different directions are shown in Fig. 2(d). As expected [10], the Hall conductivity is $\sigma_0 = \frac{e^2}{\pi h} k_0 = \frac{e^2}{2h}$ when ϵ_F is aligned with the

Weyl points. From the perspective of the discrete manifold, this can be understood by noticing $\mathbf{k}_{n,p} \approx (\pm \frac{\pi}{2}, 0, 0)^T$, which can be factored out when $\epsilon_F \rightarrow 0$. The summation in Eq. (9) then becomes the total flux of the Berry curvature evaluated on two spheres ($\phi_\pm = \pm 2\pi$) weighted by constants $\pm k_0$, respectively. Numerically, the spheres are resolved as two tetrahedra at the limit of $\epsilon_F \rightarrow 0$. However, since these tetrahedra remain homeomorphic with spheres, the numerical evaluation of the Berry-curvature flux is only determined by the number of sources or drains enclosed. This allows for precise numerical results when ϵ_F is arbitrarily close to the Weyl points. Using Eq. (11), one can obtain all the elements of the spin Hall conductivity tensor $\sigma_{\mu\nu}^{(\alpha)}$, as shown in Figs. 2(e)–2(g). This suggests that s_x has a spin Hall effect when transporting in the y - z plane. Such spin Hall effect is only allowed when ϵ_F is shifted away from the Weyl points.

The idea of a discrete quantum manifold can be directly applied for *ab initio* models. Here we demonstrate such application on the full-band model of zinc-blende GaAs. The model is obtained using a spin-polarized first-principles calculation with the projector augmented wave pseudopotential [11] implemented in Vienna *ab initio* simulation package (VASP) [12,13]. The primitive unit cell of the face-centered cubic lattice contains one Ga atom and one As atom. The corresponding Brillouin zone is sampled with a Γ -centered $7 \times 7 \times 7$ grid and an energy cutoff of 500 eV is applied for the plane-wave expansion. The generalized gradient approximation (GGA) is applied using the Perdew-Burke-Ernzerhof (PBE) form [14] as the exchange-correlation functional to obtain the Kohn-Sham eigenstates. A partially self-consistent *GW* approximation [15–17] is employed to obtain the quasiparticle energies from the fixed eigenstates. Spin-orbit coupling is included. To construct the tight-binding Hamiltonian in a Wannier-function (WF) basis, we performed a unitary transformation [6] implemented in WANNIER90 [18]. Time-reversal and other symmetries of the tight-binding model are enforced by using the package TB models [19]. The tight-binding Hamiltonian has the same exact energies as those obtained from VASP in the energy window from the lowest eigenvalues to 3.5 eV above the Fermi energy.

The band structure of zinc-blende GaAs is shown in Fig. 3(a), where the valence band splits into heavy-hole, light-hole and split-off bands due to SOC. Each band contains a twofold Kramers degeneracy. The Fermi surfaces at $\epsilon_F = \epsilon_V - 0.02$ eV are shown in Figs. 3(b)–3(e), with the vertices colored by the k_z -weighted Berry curvature evaluated as $\phi_p k_{p,z} / \delta s_p \approx (\boldsymbol{\Omega} \cdot d\hat{s}) k_z$. Here, δs_p is the total area of the triangles surrounding vertex p , whereas $d\hat{s}$ is the normal direction of the Fermi surface at the continuous limit. As expected, the Hall conductivities given by the Kramers pairs have opposite signs and exactly cancel each other. However, since the Kramers pairs have opposite spins as shown in Figs. 3(f)–3(i), the spin Hall conductivity should be finite. This is consistent with previous results [20–22]. Here, the spins of the Kramers pairs are reoriented by diagonalizing $\gamma_z = \mathbf{I} \otimes s_z$ within the degenerate subspace. The updated eigenstates are then sorted based on the eigenvalues of γ_z [23]. Such operation is necessary because arbitrary superpositions within Kramers degeneracy result in arbitrary spin directions, and the spin

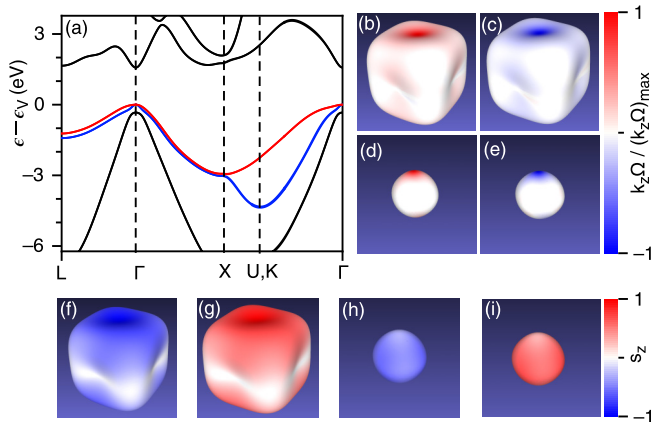


FIG. 3. (a) The band structure of GaAs along high-symmetry points. Both the heavy hole (red) and the light hole (blue) bands are twofold degenerate. [(b)–(e)] The 3D discrete quantum manifold of the Fermi surface at $\epsilon = \epsilon_V - 0.02$ eV. (b) and (c) correspond to the heavy hole band, whereas (d) and (e) correspond to the light hole band. [(f)–(i)] The electron spin s_z illustrated on the Fermi surfaces corresponding to (b)–(e), respectively.

Hall effect is thus ill-defined. In experiments, the choice of the spin direction is determined by the measurement setup. With the spins properly oriented for the Kramers pairs, the (spin) Hall conductivities at different positions of ϵ_F are illustrated in Fig. 4(a). As ϵ_F shifts deeper into the valence band, k_F increases for all Fermi surfaces, therefore the magnitude of $\sigma_{xy}^{(z)}$ also increases.

Although spins are required to properly orient for the spin Hall effect, such a requirement is not necessary for the anomalous Hall effect. Without diagonalizing the spin, the degenerate eigenstates are randomly ordered. Here we show that the order does not affect the anomalous Hall conductivity evaluated by the discrete quantum manifold. Due to Kramers degeneracy, each piece of the Fermi surface contains two coincident triangles in k space. We label these triangles Δ_{123} and Δ_{456} as shown in Fig. 4(b). Here, $(|1\rangle, |4\rangle)$, $(|2\rangle, |5\rangle)$ and $(|3\rangle, |6\rangle)$ correspond to three Kramers pairs. These pairs must be protected by an antiunitary transformation \mathcal{K} , such that $|1\rangle = |\mathcal{K}4\rangle$, $|2\rangle = |\mathcal{K}5\rangle$, and $|3\rangle = |\mathcal{K}6\rangle$. As a result, $\langle 1|2\rangle = \langle \mathcal{K}4|\mathcal{K}5\rangle = \langle 4|5\rangle^*$, hence $w_{12} = -w_{45}$. Such relation holds for all coinciding edges of the two triangles, and therefore $\phi_{123} = w_{12} + w_{23} + w_{31} = -(w_{45} + w_{56} + w_{64}) = -\phi_{456}$. Without losing generality, we swap $|3\rangle$ and $|6\rangle$, such that the two triangles become Δ_{126} and Δ_{345} , as illustrated in Fig. 4(c). Thus $\langle 2|6\rangle = \langle \mathcal{K}5|6\rangle = \langle 5|\mathcal{K}6\rangle^* = \langle 5|3\rangle^*$, such that $w_{26} = -w_{53}$. Similarly, $w_{61} = -w_{34}$, and hence $\phi_{126} = -\phi_{345}$. Note that in general, $\phi_{123} \neq \phi_{126}$ and $\phi_{456} \neq \phi_{345}$. However, since $\phi_{123} + \phi_{456} = \phi_{126} + \phi_{345} = 0$, the anomalous Hall conductivity is strictly suppressed. This can be seen from Figs. 4(d) and 4(e) where the local Berry phases are illustrated by the vertex colors. Although the Berry phases for each branch of the degenerate bands are assigned randomly, their contributions to the anomalous Hall conductivity add to zero, as shown by the red line in Fig. 4(a).

The Fermi-surface approach has better numerical accuracy compared to the Fermi-sea approach, especially when ϵ_F is close to the singularities. We demonstrate this by setting

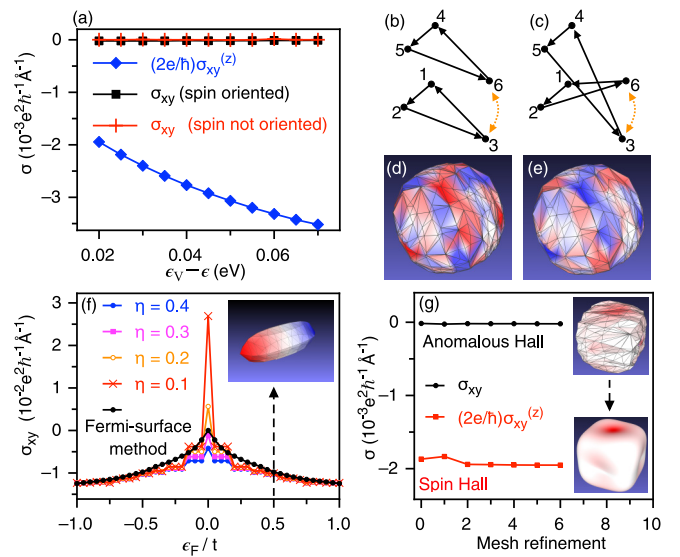


FIG. 4. (a) The anomalous Hall conductivity (dark) and the intrinsic spin Hall conductivity (blue) near the valence band top of zinc-blende GaAs. The red line denotes the Hall conductivity without orienting the spins of degenerate states. (b) Two coincident triangles due to Kramers degeneracy. The illustration is shifted for demonstration. (c) Swapping one Kramers pair in the triangle. (d-e) The discrete heavy-hole Fermi surface at $\epsilon_F = \epsilon_V - 0.02$ eV without orienting the degenerate spins. The vertex color illustrates the local Berry phases ϕ_p . (f) Comparison between the Fermi-sea and the Fermi-surface results. The inset shows the Fermi-surface at $\epsilon_F = 0.5t$. (g) The convergence of numerical results after mesh refinements. The insets compare the zeroth and the sixth refinement for the heavy-hole band of GaAs.

$k_0 = 0$ in Eq. (12) such that the two Weyl points merge at Γ point, and the Hall conductivity should be zero when $\epsilon_F = 0$. For simplicity the k values are based on the lattice constant of 1\AA . Using the Fermi-sea approach, the anomalous Hall conductivity is given by $\sigma_{yz} = \frac{e^2}{h} \left(\frac{1}{2\pi}\right)^3 \int_{\epsilon < \epsilon_F} \Omega_{x,n} d^3v$, where $\Omega_{x,n} = -2\text{Im} \sum_{m \neq n} \frac{\langle n_{\mathbf{k}} | \partial_{k_x} H | m_{\mathbf{k}} \rangle \langle m_{\mathbf{k}} | \partial_{k_z} H | n_{\mathbf{k}} \rangle}{(\epsilon_{n,\mathbf{k}} - \epsilon_{m,\mathbf{k}})^2 + \eta^2}$. Here, a finite η has to be included in the denominator to avoid singularity. Using a $32 \times 32 \times 32$ mesh, the Fermi-sea results are compared to the Fermi-surface one in Fig. 4(f). When ϵ_F is away from the merged Weyl point, both approaches obtain similar results. However, σ_{yz} encounters a singularity at $\epsilon_F = 0$, and varies significantly with η . This is not an issue for the Fermi-surface approach, where σ_{yz} smoothly reduces to 0. Another advantage of the Fermi-surface approach is a better scalability. Since it only involves vertices near ϵ_F , the time complexity scales as $O(n^2)$, where n is the linear mesh density. On the contrary, the Fermi-sea approach scales as $O(n^3)$, since the mesh needs to resolve a 3D volume. To demonstrate the numerical stability of the Fermi-surface approach we compare the (spin) Hall conductivities of GaAs at different levels of surface-mesh refinement [Fig. 4(g)]. For simplicity the Fermi surface is uniformly refined, where the number of triangles doubles after each refinement.

The method introduced in this paper has been focusing on bulk materials only. In principle, such approach is also suitable for 2D materials, since one can introduce a third

parameter λ_z , such that $H(k_x, k_y, \lambda_z)$ is periodic in all three dimensions [24,25]. The intrinsic (spin) Hall conductivity will then be obtained “per thickness,” treating the new parameter as the k_z dependency similar to the case of a bulk. Although the Fermi surfaces demonstrated in this letter are only resolved in spin, the method can, in principle, resolve the Hall conductivity in any local properties of the Fermi surface such as the angular momentum. New types of Hall effects can thus

be straightforwardly evaluated, suggesting the rich physics to further explore.

Work at UNH was supported by U.S. Department of Energy, Office of Science, Basic Energy Sciences under No. DE-SC0020221. First-principles calculations were conducted on Extreme Science and Engineering Discovery Environment (XSEDE) under Grant No. TGPHY170023.

-
- [1] N. Nagaosa, J. Sinova, S. Onoda, A. H. MacDonald, and N. P. Ong, *Rev. Mod. Phys.* **82**, 1539 (2010).
- [2] D. Xiao, M.-C. Chang, and Q. Niu, *Rev. Mod. Phys.* **82**, 1959 (2010).
- [3] Y. Yao, L. Kleinman, A. H. MacDonald, J. Sinova, T. Jungwirth, D.-s. Wang, E. Wang, and Q. Niu, *Phys. Rev. Lett.* **92**, 037204 (2004).
- [4] X. Wang, J. R. Yates, I. Souza, and D. Vanderbilt, *Phys. Rev. B* **74**, 195118 (2006).
- [5] G. Y. Guo, S. Murakami, T.-W. Chen, and N. Nagaosa, *Phys. Rev. Lett.* **100**, 096401 (2008).
- [6] N. Marzari and D. Vanderbilt, *Phys. Rev. B* **56**, 12847 (1997).
- [7] F. D. M. Haldane, *Phys. Rev. Lett.* **93**, 206602 (2004).
- [8] X. Wang, D. Vanderbilt, J. R. Yates, and I. Souza, *Phys. Rev. B* **76**, 195109 (2007).
- [9] D. Gosálbez-Martínez, I. Souza, and D. Vanderbilt, *Phys. Rev. B* **92**, 085138 (2015).
- [10] K.-Y. Yang, Y.-M. Lu, and Y. Ran, *Phys. Rev. B* **84**, 075129 (2011).
- [11] P. E. Blöchl, *Phys. Rev. B* **50**, 17953 (1994).
- [12] G. Kresse and J. Furthmüller, *Comput. Mater. Sci.* **6**, 15 (1996).
- [13] G. Kresse and J. Furthmüller, *Phys. Rev. B* **54**, 11169 (1996).
- [14] J. P. Perdew, K. Burke, and M. Ernzerhof, *Phys. Rev. Lett.* **77**, 3865 (1996).
- [15] M. S. Hybertsen and S. G. Louie, *Phys. Rev. B* **34**, 5390 (1986).
- [16] M. Shishkin and G. Kresse, *Phys. Rev. B* **74**, 035101 (2006).
- [17] M. Shishkin and G. Kresse, *Phys. Rev. B* **75**, 235102 (2007).
- [18] A. A. Mostofi, J. R. Yates, G. Pizzi, Y.-S. Lee, I. Souza, D. Vanderbilt, and N. Marzari, *Comput. Phys. Commun.* **185**, 2309 (2014).
- [19] D. Gresch, Q. S. Wu, G. W. Winkler, R. Häuselmann, M. Troyer, and A. A. Soluyanov, *Phys. Rev. Mater.* **2**, 103805 (2018).
- [20] G. Y. Guo, Y. Yao, and Q. Niu, *Phys. Rev. Lett.* **94**, 226601 (2005).
- [21] X.-L. Qi, Y.-S. Wu, and S.-C. Zhang, *Phys. Rev. B* **74**, 085308 (2006).
- [22] S. Murakami, N. Nagaosa, and S.-C. Zhang, *Science* **301**, 1348 (2003).
- [23] I. V. Solovyev, V. V. Mazurenko, and A. A. Katanin, *Phys. Rev. B* **92**, 235109 (2015).
- [24] S. Ryu, A. P. Schnyder, A. Furusaki, and A. W. W. Ludwig, *New J. Phys.* **12**, 065010 (2010).
- [25] A. M. Turner, Y. Zhang, R. S. K. Mong, and A. Vishwanath, *Phys. Rev. B* **85**, 165120 (2012).